Utilizing Interlayer Excitons in Bilayer WS_2 for Increased Photovoltaic Response in Ultrathin Graphene Vertical Cross-Bar Photodetecting Tunneling Transistors

Yingqiu Zhou,[1] Haijie Tan,[1] Yuewen Sheng,[1] Ye Fan,[2] Wenshuo Xu,[1] Jamie H. Warner[1]*

[1]Department of Materials, University of Oxford, Parks Road, Oxford, OX1 3PH, United Kingdom

[2]Electrical Engineering Division, Department of Engineering, University of Cambridge, 9 JJ Thomson Avenue, Cambridge, CB3 0FA, United Kingdom

*Jamie.warner@materials.ox.ac.uk;

Abstract

Here we study the layer dependent photoconductivity in Gr/WS_2/Gr vertical stacked tunneling (VST) cross-bar devices made using 2D materials all grown by chemical vapor deposition. The larger number of devices (>100) enables a statistically robust analysis on the comparative differences in the photovoltaic response of monolayer and bilayer WS_2, which cannot be achieved in small batch devices made using mechanically exfoliated materials. We show dramatic increase in photovoltaic response for Gr/WS_2(2L)/Gr compared to monolayers because of the long inter- and intra-layer exciton lifetimes, and the small exciton binding energy (both interlayer and intralayer excitons), of bilayer WS_2 compared with that of monolayer WS_2. Different doping levels and dielectric environments of top and bottom graphene electrodes results in a potential difference across ~1nm vertical device, which gives rise to large electric

fields perpendicular to the WS_2 layers that cause band structure modification. Our results show how precise control over layer number in all 2D VST devices dictates the photo-physics and performance for photo-sensing applications.

KEYWORDS: WS_2, graphene, heterostructures, photodetectors, vertical stacked heterostructures, 2D materials

Two-dimensional (2D) materials, which can be single or few atoms thick are promising candidates for next-generation ultrathin electronics and optoelectronics devices, due to their unique electrical,[1,2] thermal,[3] and mechanical properties.[4,5] Graphene, a single layer of sp^2 bonded carbon atoms, has high carrier mobility,[6] is relatively chemically inert[7] and has good mechanical flexibility[8,9] that make it useful for flexible electronics and as an electrode material for ultrathin 2D devices. With regard to these properties, graphene has found a host of applications, ranging from chemical[10,11] and strain sensors[12,13] to transistors.[14] However, graphene has a low absorption of light, only 2.3% in the range of visible range as a photodetector. This follows from the absence of an intrinsic bandgap.[15] Although a band-gap can be induced externally in graphene through high strain or electric field,[16-18] such approaches are energy-consuming and less practicable for application compared to direct band gap semiconductors.

Transition metal dichalcogenides (TMDs), such as MoS_2 and WS_2 are recent 2D materials with an intrinsic bandgap, and for this reason have been intensively studied as photodetectors.[19,20] Among them, WS_2 is very appealing due to its chemical and thermal stability,[21] tunable band-gap ranging from visible to UV,[22] large crystal size and possibility of forming uniform films using chemical vapor deposition (CVD).[23] A promising approach is to combine graphene with TMDs to make use of both their unique properties: graphene's semi-metallic band structure with work-function tunability used as a contact electrode and semiconducting TMDs as the active absorbing

material in photodetectors. Several reports have demonstrated devices with graphene (Gr) as an electrode,[24–26] resulting in substantial improvements achieved in photocurrents under applied gate potential. Due to its ultrathin nature, there are two configurations graphene can be used to contact TMD devices: (a) lateral planar structures, where TMDs are contacted by co-planar graphene electrodes to form lateral devices.[24,27] (b) vertically stacked heterostructures, where TMDs are sandwiched between vertically stacked graphene electrodes.[28-30] The different configurations of the graphene electrodes lead to variances in the mechanisms governing electrical conductance and photocurrent generation. Vertically stacked heterostructures involve tunneling between layers and offer the largest surface area for interfacing between two layered materials, which is ideal for photo-sensing applications.

Most all-2D vertical stacked heterostructure devices explored for photodetector applications so far have been based on mechanical exfoliated 2D crystals, which severely limits production yield and device fabrication scalability. The small batch numbers from devices made with mechanically exfoliated 2D materials makes it difficult to obtain statistically robust results, given variances in device to device behaviors. Moreover, it is challenging to control the number of layers of TMD crystals isolated by mechanical exfoliation with most regions having mixtures of both mono- and bi-layers. The rise of high quality CVD grown 2D TMDs and graphene offers a possible route to explore the wafer scale fabrication of all-2D opto-electronic devices and the assessment of their performance, which is essential for the industrial realization of 2D technology. Here, we show Gr/WS_2/Gr based ultrathin photodetectors fabricated entirely using CVD grown materials. In particular we utilize vertically stacked cross-bar graphene electrodes to enable large numbers of devices to be fabricated with minimal alignment steps. We systematically study the properties of such devices with monolayer and bilayer WS_2 sandwiched between graphene

electrodes as photodetectors and reveal unique photovoltaic response in bilayer WS_2, which is observed to be one order of magnitude higher than in monolayer WS_2 device.

Results and Discussion

The fabrication process for the Gr/WS_2/Gr vertical heterostructure device is schematically illustrated in Figure 1(a). In brief, the monolayer graphene film was first synthesized by the chemical vapor deposition method and then transferred onto a silicon wafer covered with 300 nm SiO_2. The graphene film was then patterned with electron-beam lithography (EBL) and etched into strips of 20 μm width by oxygen plasma to form the bottom graphene electrode (Step1, Figure 1(a)). A layer of CVD grown WS_2 domains was then transferred onto the graphene strips as the photo-absorbing semiconductor material (Step2, Figure 1(a)). The high domain density ensures that a large number of devices are created. This approach is not aimed at producing uniform 2D arrays of devices, but instead enough devices to obtain a statistically robust analysis. Another layer of pre-patterned monolayer graphene strips was subsequently transferred on top of the substrate/Gr/WS_2 as the top electrode with a perpendicular alignment to the bottom graphene strips (Step3, Figure 1(a)). Finally bond pads (Cr/Au (10 nm/80 nm)) were patterned using EBL and thermally evaporated on the graphene electrodes (Step4, Figure 1(a)). In the center of Figure 1(a) is the 3D schematic illustration showing the typical device geometry with graphene top and bottom cross bar electrodes and WS_2 sandwiched in between. In this paper, we only studied the vertical devices with top and bottom graphene completely separated by WS_2 domains. As shown in the SEM image (see Figure 1(b)) our CVD synthesized WS_2 are mainly isolated domains evenly distributed across the 1 cm×1 cm substrate. The WS_2 crystals consist of both monolayer and bilayer domains, which enables the study of layer dependence on the device performance. The fabrication of vertical graphene cross bar electrode pairs was highly reproducible, with ~95% yield.

The high density of WS_2 domains resulted in ~50% of graphene cross bar electrode pairs to be separated by WS_2 to form Gr/WS_2/Gr devices, with the majority of WS_2 crystals being monolayer (90%) and a small number bilayer (10%). Figure 1(c) shows the SEM image of a typical Gr/WS2/Gr device. The devices were then isolated from other devices by mechanical etching of the surrounding graphene strips using a nanotip probe to stop any leakage (figure S5).

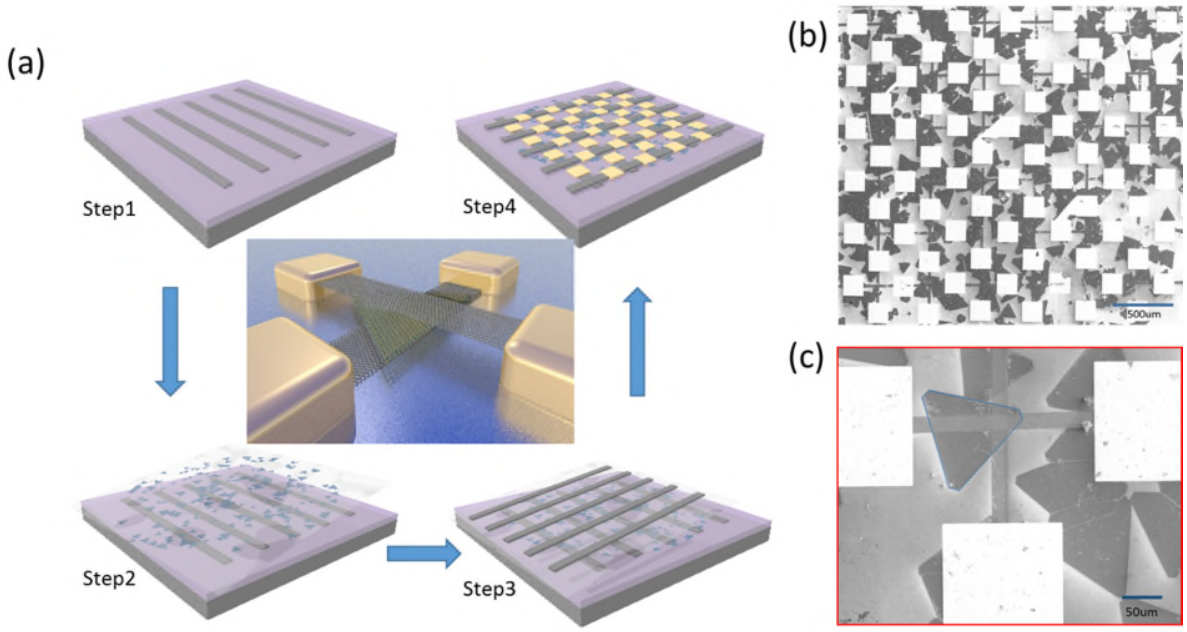

Figure 1. (a) Schematic illustration showing the fabrication steps (Step1-Step4) for creating the vertically stacked Gr/WS_2/Gr devices. Step 1: Graphene nanoribbon fabrication by electron beam lithography. Step 2: Transfer of WS2 domains onto bottom graphene nanoribbons and removal of polymer. Step 3: Transfer of top graphene nanoribbon electrodes. Step 4: Deposition of Au bond pads to graphene nanoribbons at bottom and top. Each device is isolated from all others before measurement by cutting the connecting graphene electrodes using a sharp metal tip. (b) SEM image of the fabricated device array. (c) SEM image of one of the vertical devices in (b).

Figure 2(a) is an optical microscope image of a typical device that comprises a monolayer WS_2 domain sandwiched between graphene electrodes (top graphene: Gr_T, and bottom graphene Gr_B), and a bilayer WS_2 beside the device. The monolayer and bilayer WS_2 can be distinguished by the contrast from the optical images. Both the monolayer and bilayer WS_2 are further probed using Raman and photoluminescence spectroscopy. Figure 2(b) is the Raman spectrum of graphene electrodes with excitation wavelength of 532nm. It shows a 2D/G intensity ratio of around 1.5, indicating our CVD synthesized graphene is mostly monolayer.[31] The darker traces in the graphene ribbons in the optical image are bilayer graphene, Raman curve of which is shown in S3(c). The Raman spectra of monolayer and bilayer WS_2 are shown in figure 2(c). Fitting Lorentzian curves reveals the presence of multiple peaks in the Raman spectra of WS_2, $2LA$ (second-order longitudinal acoustic), $E_{2g}^1(\Gamma)$ (in-plane vibration mode) and $A_{1g}(\Gamma)$ (out-of-plane mode) (Figure 2(c)). The two main peaks $E_{2g}^1(\Gamma)$ and $A_{1g}(\Gamma)$ of monolayer WS_2 are positioned at 355.2cm^{-1} and 417.5cm^{-1}, respectively, similar to our previous report on monolayer WS_2.[24] Also, the second-order $2LA$ band is more intense than the first-order $E_{2g}^1(\Gamma)$ and $A_{1g}(\Gamma)$ bands, due to the double-resonance process.[32,33] While for the bilayer WS_2, the $E_{2g}^1(\Gamma)$ peak was softened, positioning at 355.66 cm^{-1} and $A_{1g}(\Gamma)$ upshift to 419.49 cm^{-1}. Also, the peak intensity ratio of $2LA(M)/A_{1g}(\Gamma)$ decreases from 7.6 to 5.9 as layer number increases from monolayer to bilayer. PL spectra of monolayer and bilayer WS_2 on SiO_2/Si substrate are conducted to further determine the number of layers of WS_2, as shown in figure 2(c). Bilayer WS_2 shows a significant PL quenching compared with monolayer WS_2. Figure 2(e) is the PL intensity comparison of monolayer WS_2 in two different regions, with the black curve representing the WS_2 on the SiO_2 surface, and the orange one from the WS_2 sandwiched between two graphene electrodes. The PL intensity from WS_2 is heavily quenched when in contact with graphene. The deconstruction of the PL spectra of WS_2 into

negative trion (X^-) and exciton (X) peaks using Lorentz fitting are shown in Figure S3. For the WS_2 on the SiO_2 surface, the integrated PL intensity ratio of X^-/X is 1.7 (Figure S3(c)). Upon stacking the WS_2 with graphene, the X^-/X ratio decreases to 0.6, indicating the depletion of electrons in WS_2 (Figure S3(d)). This is due to electron transferring from WS_2 to graphene (top and bottom layers) within the Gr/WS_2/Gr stacks.[34] The quenching of the PL in the stacked region is an indication of strong interactions between graphene and WS_2 layers.[34,35]

Figure2. Optical characterization of Gr/WS_2(1L)/Gr heterostructure. (a) Optical microscope image of a Gr/WS_2(1L)/Gr device. Monolayer WS_2, bilayer WS_2 and graphene are shown in the image. (b) Raman

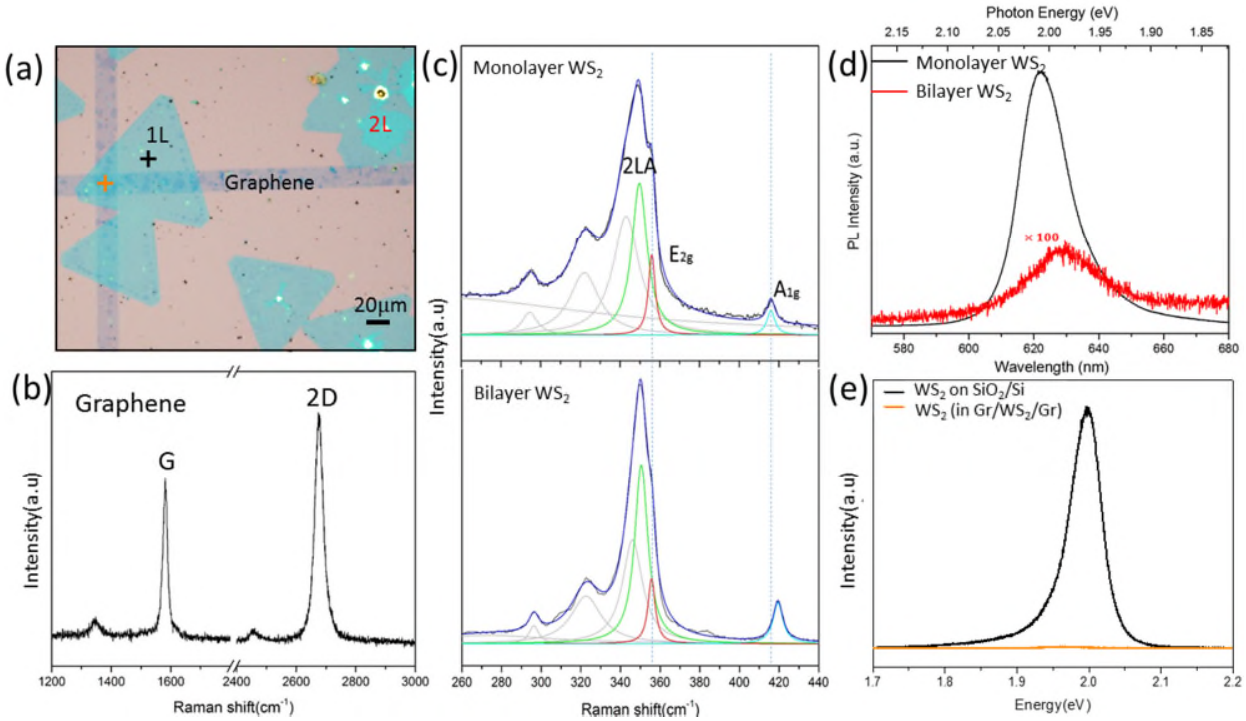

spectrum of graphene (c) Raman spectra of monolayer and bilayer WS_2 excited with 532nm wavelength laser. The two main peaks which reflect the properties of WS_2 are fitted using Lorentzian function. (c) The PL signals of monolayer and bilayer WS_2 domains on SiO_2. The bilayer WS_2 PL signal was magnified by

100 times. (e) PL spectra from monolayer WS_2 domain on SiO_2 (black) and sandwiched between graphene top and bottom electrodes (yellow).

First we measured the dark current from Gr/WS_2(1L)/Gr devices at room temperature. Figure 3(a) shows the current-voltage (I_{ds}-V_{ds}) data for a typical device with the applied bias voltage within the range of 0-1 V at different back gate voltages. The Gr/WS_2(1L)/Gr devices show linear I_{ds}-V_{ds} curves, which is typical for tunneling currents through monolayer WS_2.[36] The dependence of the photocurrent on the laser power is then studied at room temperature and in ambient condition. The bottom graphene is always grounded and the source-drain bias is applied to the top graphene electrode in our study. The optical power dependent transfer curves of Gr/Gr vertical structure devices without WS_2 inserted are shown in Figure S1. Figure 3(b) shows the transfer curves of the Gr/WS_2(1L)/Gr photodetector upon exposure to 532 nm (2.3eV) light with increasing power, with a source-drain bias voltage fixed at 0.5 V. The transfer curves show V-shape, very similar to that of pristine graphene on a SiO_2 substrate, suggesting that the carrier transport of our vertical devices is mainly dominated by the semi-metallic density of states of graphene in dark condition.[37] Without illumination, the device shows a charge neutrality point (V_{CNP}) located around 32 V. The device shows strong response to the incident light, with the increasing power gradually shifting the transfer curve towards the negative direction. The neutrality point splits into two under increasing illumination power, with one (V_{CNP1}) shifting significantly towards the negative direction while the other (V_{CNP2}) shifting only a little when the light power increases. Prior work on WS_2 vertically stacked on graphene nanoribbon transistors showed similar multiple Dirac points when illuminated due to local changes in doping levels of graphene from charge transfer.[34] The transfer of photo-excited electrons in WS_2 to graphene is also the likely cause of the shift in Dirac position (V_{CNP1}), which results in negative photocurrent for

large negative gate biases and positive photocurrents for large positive gate biases, as shown in Figure 3(c). The photocurrent was obtained by subtracting the dark current from the current when the vertical device is illuminated with light. The light green region is the photocurrent transition area, where the photocurrent reverses the sign. To be specific, when the V_g is at 20V, the photocurrent is negative with small incident laser power and reverses the sign when the laser power reaches a higher value. This is reasonable as more photo-excited electrons transfer to graphene with higher incident laser power, which combine with the holes in graphene and the remaining electrons will contribute to the photocurrent. To evaluate the performance of our device, photoresponsivity and photo-gain are analyzed, which are important figures of merit to evaluate the performance of a photodetector. Photoresponsivity is the electrical response to the incident laser power, which is expressed as:

$$R = \frac{I_{\text{ph}}}{P_{\text{laser}}} \tag{1}$$

I_{ph} is the generated photocurrent, P_{laser} is the power illuminated on the device. Figure 3(d) shows the responsivities of this photodetector with respect to the illuminated laser power at two back gate voltages (V_g=80 V, -80 V). The photoresponsivity of the device decreases linearly with increasing the excitation laser power, which is attributed to be the photo absorption saturation in monolayer WS_2 sandwiched between graphene electrodes. Photo-gain is the number of detected charge carriers per single incident photon and can be calculated by the formula:

$$G = \frac{Rhv}{e\eta_{\text{ext}}} \tag{2}$$

h is the plank constant, v is the frequency of the incident light, R is the photoresponsivity, e is the elementary charge, and η_{ext} is the external quantum efficiency. If we optimistically assume that all the incident photons on the device are extracted as charge carriers by the electrodes and

contribute to the photocurrent, which means η_{ext} is 100%. the photo-gain we calculated can be as high as 136 and 106 for our device with gate voltage at -80 V and 80 V, with laser power of 0.1μW, as shown in Figure 3(e). A lower external quantum efficiency would give rise to even higher gains in our devices and our calculations provides a conservative minimum gain. This calculation assumes the absorbance of 532nm light for monolayer WS_2 is around 8%.[38]

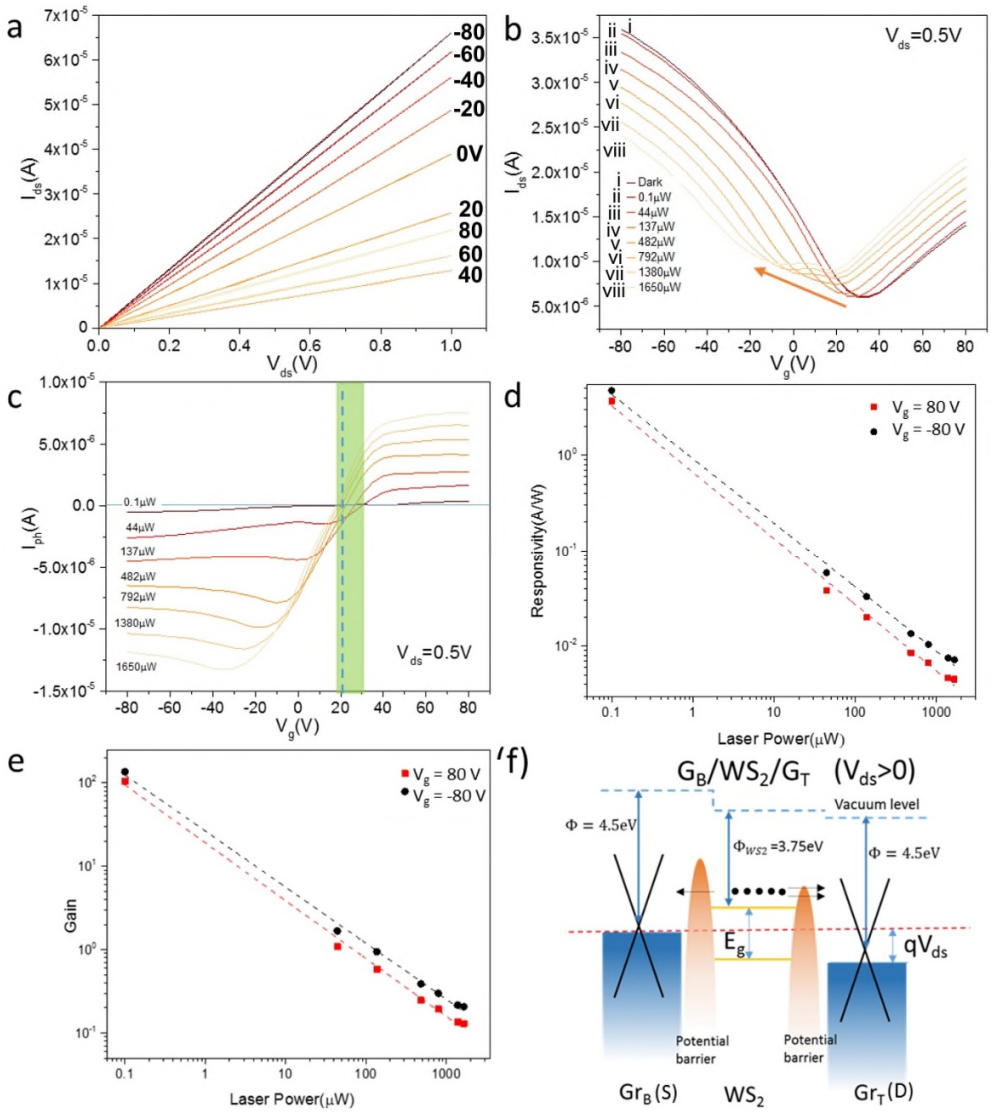

Figure 3. Photoresponse of the Gr/WS_2(1L)/Gr devices. (a) Plots the I_{ds}–V_{ds} curves of Gr/WS_2(1L)/Gr device with various gate voltages during the forward sweep in dark condition. (b) Transfer curves for the

Gr/WS_2(1L)/Gr photodetectors under the exposure of light (532nm wavelength) with increasing powers. (c) Photocurrent as a function of the back-gate voltage based on the transfer curves in (b). The light green region marks the photocurrent transition area. (d) Photoresponsivity and (e) photo-gain of the Gr/WS_2(1L)/Gr photodetector with increasing incident laser power. (f) Band diagrams of the vertical Gr/WS_2/Gr structure with positive bias voltage (Gr_B is connected to source and Gr_T is connected to drain). qVds is the fermi level difference of two graphene induced by bias voltage. The solid black dots represent the photo-excited electrons in WS_2. The orange shape is the electrostatic potential barrier formed in the vdW gap between graphene and WS_2. The black arrows represent the electrons generated in WS_2 tunnel through the potential barriers to the Gr_B and Gr_T.

We attribute the photocurrent in Gr/WS_2(1L)/Gr vertical devices mainly to be the separation and collection of photo-excited electrons and holes in WS_2. Photo-thermoelectric effects (PTEs) due to different thermoelectric power in graphene-based photodetectors has been explored,[50,51] but this effect is negligible in our devices due to the low excitation powers, which will be discussed in details when we study the Gr/WS_2(2L)/Gr vertical devices in the following part. Because of the van der Waals (vdW) gap between graphene and WS_2, tunneling potential barriers are formed in Gr_B/WS_2 and WS_2/Gr_T interfaces, we assume the barrier widths between Gr_B/WS_2 and WS_2/Gr_T are the same, but with different heights. By creating asymmetric tunneling barrier heights between Gr_B/WS_2 and WS_2/Gr_T by variable doping and local dielectric environments, the photo-excited electrons in WS_2 have different collecting rates by Gr_B and Gr_T. The difference in electron collecting rates results in an overall photocurrent. Tunneling barrier height can be modulated by external applied bias and also the doping levels of G_B and G_T induced by the surrounding environment, as shown in Figure 3(f). The photocurrent results of Gr_B/WS_2 and WS_2/Gr_T confirm that the electrostatic potential barrier in the Gr_B/WS_2 interface is higher than that in the WS_2/Gr_T interface when there is no bias and gate voltage applied (Supporting

Information S2). The internal asymmetric potential barriers between Gr_B and Gr_T/WS_2 interfaces is similar to the results reported for Gr/MoS_2 interfaces.[29] The energy of the excited electrons in WS_2 was calculated to be 3.7eV below the vacuum energy (Supporting Information S2), located between the region confined by the top and bottom barriers.[29] In this case, the photo-generated electrons can tunnel from WS_2 through the barrier into both Gr_B and Gr_T with different probabilities, with higher tunneling probability through the lower barrier at WS_2/Gr_T interface.[29] The difference in the tunneling probabilities of the photo-excited electrons into Gr_T and Gr_B modulate the magnitude of photocurrent. As in the Gr/MoS_2 interfaces, hole tunneling from graphene electrodes to TMDs also occurs to balance overall charge distributions during photoexcitation.[29]

When examining the photoresponse behavior for devices with bilayer WS_2 we found a significant difference between $Gr/WS_2(2L)/Gr$ vertical heterostructure devices and $Gr/WS_2(1L)/Gr$ devices. The I_{ds}-V_{ds} curves of both $Gr/WS_2(1L)/Gr$ and $Gr/WS_2(2L)/Gr$ devices pass through the origin at various gate voltages in the dark condition (Supporting Information S4). As shown in Figure 4(a), when illuminated with light, the bilayer WS_2 based device shows much higher short-circuit current (I_{sc}) and open-circuit voltage (V_{oc}) (For the $Gr/WS_2(2L)/Gr$ device, $I_{sc} = 9 \times 10^{-7}$A, V_{oc} = 22mV) compared with that of $Gr/WS_2(1L)/Gr$ ($I_{sc} = 1.5 \times 10^{-8}$A, V_{oc} = 0.2mV). For the $Gr/WS_2(2L)/Gr$ devices, when the V_g decreases, there is a gradual upshift of the I_{ds}-V_{ds} curve (see Figure 4(b), illuminated with a fixed laser power). Figure 4(c) illustrates the dependence of the I_{sc} and $|V_{oc}|$ on the V_g. It shows that V_g can modulate both the I_{sc} and $|V_{oc}|$ effectively. When V_g = 0V, the I_{sc} and $|V_{oc}|$ are at around 1×10^{-6} A and 22 mV. When V_g decreases, both the I_{sc} and $|V_{oc}|$ increase to 1.3×10^{-6} A and 26 mV at -10V. When V_g increases, both I_{sc} and $|V_{oc}|$ decrease, reaching 4×10^{-7} A and 14 mV at 60V. And the decreasing slope

becomes smaller at higher V_g. It should be noted that the modulation of the photocurrent by the external gate voltage does not generate additional dark current as shown in Figure S4(c). The power of the incident light also has the ability to tune the I_{sc} and $|V_{oc}|$ of our Gr/WS_2(2L)/Gr devices, as shown in Figure 4(d). Both I_{sc} and $|V_{oc}|$ scale exponentially with incident light power and show no indication of saturation over the measured range of optical powers. From the direction of the V_{oc}, it is easy to exclude the dominance of the PTE effect in our vertical heterostructure. When V_g increases from -10 V to 60 V, the doping levels of the G_B and G_T turn from p+/p to n+/n, as shown in Figure 4(e). If PTE is the dominant mechanism of photocurrent generation, the sign of the V_{oc} should reverse when V_g passed a certain value between -10V and 60V, which has been confirmed by Gabor et.[50] To be specific, because of the substrate can dissipate heat well, the Gr_T has higher temperature than the Gr_B, which leads to the charge carriers transporting from GrT to Gr_B. So when the charge carrier changes from electrons to holes, the direction of photocurrent should reverse. This means when the V_g change from 60 V to -10 V, the But in our experiment, we observed that V_{oc} keeps moving in the negative direction as V_g is swept from 60V to -10V, which indicates that PTE is not the dominate mechanism of the photocurrent in our experiment.

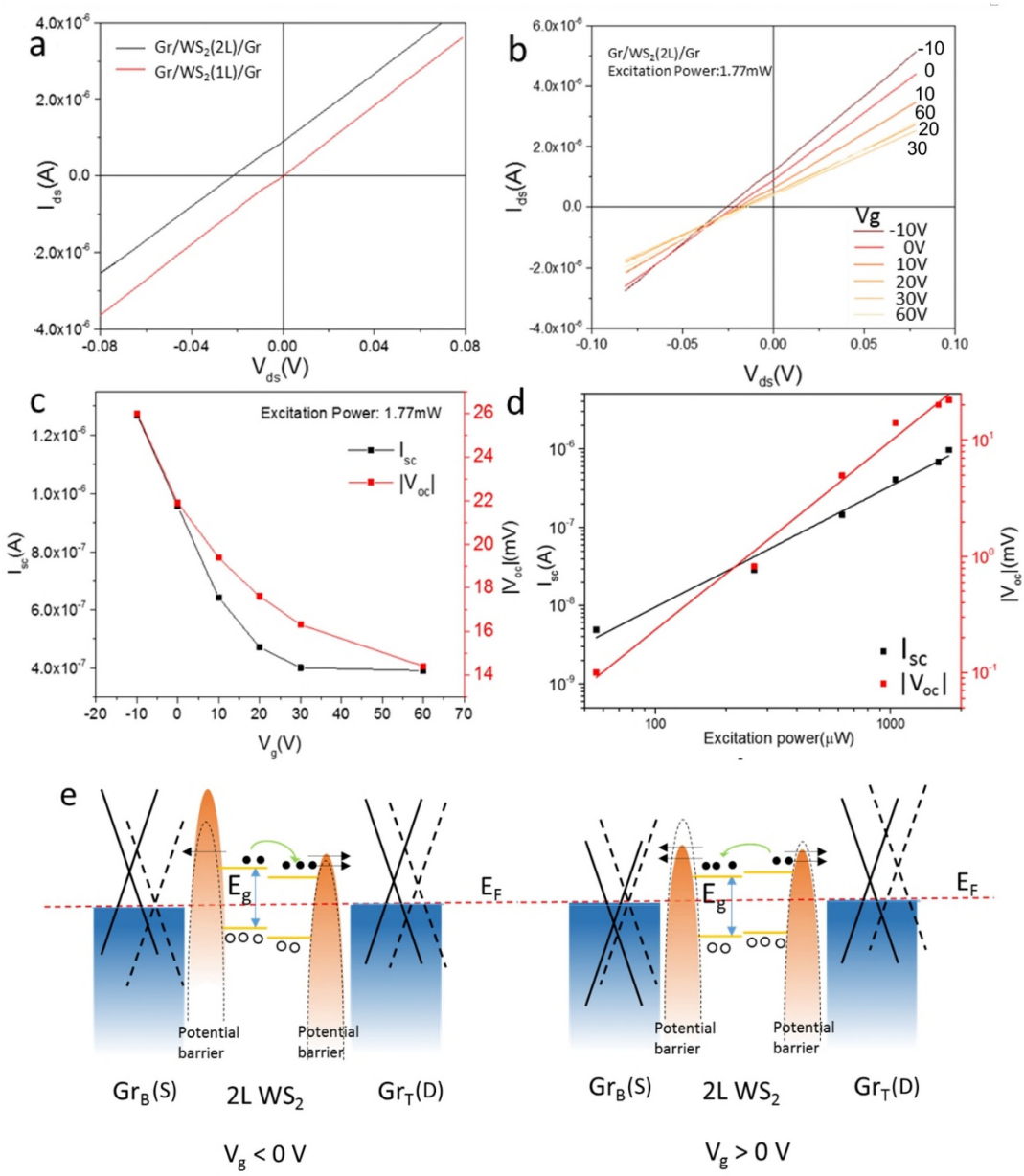

Figure 4. Photovoltaic effect of Gr/WS_2(2L)/Gr vertical devices. (a) Output characteristics of Gr/WS_2(1L)/Gr and Gr/WS_2(2L)/Gr vertical devices under 532nm illumination. (b) Output characteristics of Gr/WS_2(2L)/Gr vertical device with various back gate voltages under the excitation power at 1.77mW for 532nm. (c) The dependence of short-circuit-current (I_{sc}) and open-circuit voltage (V_{oc}) on the *V*g with

the excitation power fixed at 1.77mW for 532nm. (d) The power-law dependence of I_{sc} and $|V_{oc}|$ on the excitation power with the $V_g = 0$ V, the red dots represent $|V_{oc}|$ and black dots represent I_{sc}. The black and red lines are the fitting curves. (e)The band diagrams of Gr_B/WS_2 (2L)/Gr_T with negative (left) and positive (right) V_g and zero bias voltage. The dotted straight line and parabola represent the graphene energy band the potential barrier with zero gate voltage and bias voltage, while the solid line and parabola are the graphene energy band and potential barrier with non-zero gate voltage and zero bias voltage. The red dotted line is the fermi level of the whole device. With non-zero V_g, the bottom WS_2 feels stronger electric field compared with the top WS_2, causing an energy band offset in bilayer WS_2.

As mentioned above, Gr_T is more p-doped than the Gr_B in the vertical junction, leading to a potential difference between the two graphene electrodes in our vertical Gr/WS_2/Gr devices. When light is absorbed by the WS_2 monolayer, e-h pairs are generated, with around 60% of the free electrons and holes rapidly bound into excitons, on time scales shorter than 1 ps.[40,41] So the photocurrent in our devices is mainly dependent on the exciton dissociation. The exciton binding energy of monolayer WS_2 is as high as 0.71 eV at room temperature over a magnitude order than conventional semiconductors.[42,43] The large binding energy of excitons in monolayer WS_2 suppresses the separation of e-h pairs and thus the number of free charge carriers contributing to the photocurrent is small without applied bias voltage. The e-h pairs in monolayer WS_2 also rapidly recombine across the direct band gap.[42,44] So the I_{sc} we observed in the monolayer WS_2 vertical devices is rather small.

The reason for the high I_{sc} and $|V_{oc}|$ in the bilayer WS_2 vertical devices is first due to the increased absorbance of light in bilayer WS_2 compared with its monolayer counterpart. So the generated I_{sc} in bilayer vertical devices should be at most two times that generated in monolayer WS_2 devices if we only considered the absorbing differences in bilayer WS_2. The average I_{sc} we measured in bilayer WS_2 vertical devices is 10 times of that in monolayer WS_2 devices (supporting

information S3), so there must be other factors which contribute to the increased I_{sc} in bilayer WS_2 vertical devices. We attribute the high I_{sc} to an increased efficiency of exciton dissociation in bilayer WS_2 compared to monolayers, which is ascribed to two reasons. (i) Lower exciton binding energy in bilayer WS_2, which is half of that in monolayer WS_2.[46] This enables higher probability of exciton dissociation and thus higher I_{sc} and $|V_{oc}|$. (ii) Longer exciton life time in bilayer WS_2. The lifetime of intralayer excitons is longer than that of excitons in monolayer WS_2, because bilayer WS_2 has an indirect band gap. The momentum conservation requires extra phonons for the recombination of exciton in bilayer WS_2. Fast dissociation time was observed in few layer MoS_2 (700fs), which is much shorter than that for excitons in monolayer MoS_2 (60ps).[47]

The V_g dependence of the I_{sc} and $|V_{oc}|$ in the Gr/WS_2 (2L)/Gr vertical devices is explained using the energy band shift in Figure 4(e). By applying negative (positive) V_g on our devices, both Gr_B and bottom WS_2 layer are more influenced by the gate voltage due to closer proximity, inducing stronger p-doping effect (n-doping) than the top WS_2 and Gr_T. This could cause an energy band offset between the bottom and top WS_2 layers in bilayer WS_2, similar to the effect of an external electric field induced energy band offset in bilayer MoS_2 proposed by Chu et.al.[39] The value of band offset represents the electric field strength applied on the bilayer WS_2. The two layers in bilayer WS_2 are strongly coupled as they are grown directly by a CVD process rather than being assembled manually by a layer-by-layer transfer.[45] Similar to the heterostructure, the staggered band of bilayer WS_2 enables a quick dissociation of photo-generated intra-layer excitons to free carriers (electrons and holes).[25] The interlayer excitons formed between two layers of WS_2 also have a low binding energy, with a similar value of binding energy to that of intralayer excitons when the applied electric field is at a low value.[48] The lifetime of the interlayer exciton in the $MoSe_2$/WSe_2 heterostructure is as long as 1.8ns, because of the low exciton energy and its spatially

indirect nature, even when the lifetime of the intralayer exciton in monolayer $MoSe_2$ and WSe_2 is short.[49] So in our bilayer WS_2 devices, the out-of-plane interlayer exciton is also assumed to have a long lifetime on the order of ns, which is much longer than the lifetime of excitons in monolayer WS_2. The low PL signal of WS_2 bilayers between two graphene sheets prevents direct measurements of the signals. When applying negative gate voltage, the conduction band minimum (CBM) and valance band maximum (VBM) of bottom layer WS_2 shift higher than that of bottom WS_2. The tunneling barrier difference between Gr_B/WS_2 and Gr_T/WS_2 is also enlarged. This band-offset facilitates the electron and hole transfer to the top and bottom WS_2 respectively, leading to more electrons tunneling to the top graphene and less to the bottom graphene. So the net photocurrent increases with negative gate voltage. The explanation is the same as applying positive gate voltage.

Conclusion

In summary, we have realized the large scale fabrication of ultrathin $Gr/WS_2/Gr$ cross bar photo-detecting transistor device. All the materials used in the devices are synthesized by CVD methods with large domain sizes and relatively homogeneous layer number within each domain, enabling comparisons of monolayer and bilayer crystals. The Gr/WS_2(1L)/Gr devices show high photo-gain reaching around 136 when illuminated with 532 nm light (V_g = -80 V). With the Gr_T more p-doped than the Gr_B, the Gr/WS_2(2L)/Gr devices exhibit remarkable photovoltaic effect but no obvious photovoltaic effect for Gr/WS_2(1L)/Gr devices. We attribute the difference to the small binding energy and long life time of excitons in bilayer WS_2 which contribute more free charge carriers for the photovoltaic effect. With changing the back gate voltage, the photovoltaic effect can be tunable in the Gr/WS_2(2L)/Gr devices. Our finding reveals the importance of controlling the number of layers of sandwiched photoactive material in the vertical devices.

Experimental Methods

CVD Synthesis of Monolayer Graphene and WS_2: WS_2 was synthesized with a two furnaces system to control the temperature of S and WO_3 separately. A 2×2 cm silicon chip with 300 nm SiO_2 on top was used as the growth substrate. The substrate was first sonicated in acetone for 15 min, then in 2-propanol for another 15 min, followed by O_2 plasma for 15 min. After being cleaned, both the substrate and precursors were put into reaction tubes. 300 mg sulfur powder (≥99.5%, Sigma-Aldrich) was put in the outer tube (inner diameter was 22 mm) while the substrate was 40.5 cm from S powder at the downstream of the same tube. Another precursor, 200 mg WO_3 powder (≥99.5%, Sigma-Aldrich) in the inner tube (inner diameter was 12 mm), was 8.5 cm away from the substrate. The tube with precursors and substrate inside was then put into the two furnaces, with S in the center of the first furnace while WO_3 in the center of the second one. Before reaction started, system was flushed with 500 sccm Ar for at least 30 min to remove the air inside. Then the first and second furnaces were set to ramp to 180℃ and 1170℃ at their maximum rising speed, respectively. The reaction process lasted for 3 min with Ar flowed at 250 sccm and the two furnaces stable at their set temperatures. 3 min later, reaction was stopped by decreasing the flow rate of Ar to 10 sccm, meanwhile, the first furnace was heated at the maximum rising speed to 450℃ to evaporate the rest S and the second one was cooled to room temperature at its maximum cooling speed. When the temperature of second furnace decreased to 950℃, the rest S was blown by Ar at a flow rate of 500 sccm.

For the synthesis of graphene, a piece of copper foil was first polished by Brasso for 15 min and sonicated in diluted hydrochloric acid solution (HCl, 1 mol/L) to remove the residues on the copper surface. After this, the copper foil was sonicated in acetone and isopropanol (IPA) for 5 min to remove the organic residues. The copper was then placed in a 4 inch reaction tube. To ensure the uniformity of temperature during the whole growth process, the copper foil was positioned in the centre of the furnace. 1% methane in argon (CH_4), 25% hydrogen in argon (H_2) and 100% argon (Ar) were used during the flushing and graphene synthesis process. Before the reaction started, the

system was flushed with 1000 sccm Ar, 500 sccm H_2 and 50 sccm CH_4 for 30 min to remove the air inside the tube. After the flushing, the furnace was ramped to 1060 ℃ with the rising speed of 50 ℃/min accompanying with a flow of 600 sccm Ar and 300 sccm H_2. When the temperature reached the set value, the whole system remained the same condition to anneal the copper foil for 1 h. After the annealing process, the synthesis process lasted for 1 h at 1060 ℃ with the flow of 600 sccm Ar, 100 sccm H_2 and 20 sccm CH_4. The reaction was stopped by moving away the furnace from the sample position for the sample to be fast cooled to room temperature.

Transfer of CVD Synthesized Monolayer Graphene and WS_2: The graphene was synthesized on copper foil. A layer of Poly (methyl methacrylate) (PMMA) was spin-coated on graphene/Cu foil as the transfer medium. The Cu foil was then etched by the $(NH_4)_2S_2O_8$ solution (0.2 mol/L). The PMMA/graphene film was then transferred onto deionized water for three times (30 min each time) to remove the remaining $(NH_4)_2S_2O_8$. The WS_2 was synthesized on SiO_2/Si wafer. The PMMA/WS_2 film was separated from the substrate by etching the SiO_2 with KOH solution (1 mol/L). After rinsing, the floating PMMA/graphene and PMMA/WS_2 film were scoped with clean SiO_2/Si substrate and dried overnight at room temperature. Before soaked in acetone to remove PMMA, the samples were heated at 180 ℃ and 150 ℃ for 15 min for better adhesion for PMMA/graphene and PMMA/WS_2, respectively.

Device Fabrication: For making graphene electrodes, one layer of positive photoresist was spin-coated on top of graphene before the spin-coating of a layer of negative photoresist to ensure the clean surface of graphene. JEOL 5500 FS electron beam lithography system was used to write the designed pattern and followed by etching graphene with reactive ion etching (RIE). For making metal pads, bilayer of positive photoresists were used and Cr (10nm)/Au (80nm) were deposited using thermal evaporator, followed by the overnight lift-off in acetone at room temperature.

Opto-electrical Characterization of Gr/WS_2/Gr Devices: A Keithley 2400 source meter was used for the electrical measurement. Before we measured one Gr/WS_2/Gr device, we used a probe tip to break the graphene electrodes connected to other devices to isolate the one we measure. For the

opto-electrical measurement of our devices, we used a 532 nm diode-pumped solid state laser (Thorlabs, DJ532-40) which was coupled into a confocal microscope to form a beam with spot size of ~150 μm^2 as a light source. Si was used as the back gate, and bottom graphene was grounded when we did all the measurements.

Acknowledgements

JHW thanks the Royal Society and the European Research Council (Grant No: 725258 CoG 2016 LATO) for support.

Supporting Information

Photoresponse study of Gr/Gr vertical device, doping level analysis of graphene electrodes, optical characterization of bilayer WS_2, output characterization of other vertical stacked devices, cutting of device contacts.

Reference

(1) Das Sarma, S.; Adam, S.; Hwang, E. H.; Rossi, E. Electronic Transport in Two-Dimensional Graphene. *Rev. Mod. Phys.* **2011**, *83*, 407–470.

(2) Wang, Q. H.; Kalantar-Zadeh, K.; Kis, A.; Coleman, J. N.; Strano, M. S. Electronics and Optoelectronics of Two-Dimensional Transition Metal Dichalcogenides. *Nat. Nanotechnol.* **2012**, *7*, 699–712.

(3) Zhang, G.; Zhang, Y.-W. Thermal Properties of Two-Dimensional Materials. *Chinese Phys. B* **2017**, *26*, 34401.

(4) Zhang, R.; Cheung, R. Mechanical Properties and Applications of Two-Dimensional Materials. *Two-dimensional Mater. Charact. Potential Appl.* **2016**.

(5) Liu, K.; Wu, J. Mechanical Properties of Two-Dimensional Materials and Heterostructures. *J. Mater. Res.* **2016**, *31*, 832–844.

(6) Geim, A. K; Novoselov, K. S. The Rise of Graphene. *Nat. Mater.* **2007**, *6*, 183–191.

(7) Blake, P.; Brimicombe, P. D.; Nair, R. R.; Booth, T. J.; Jiang, D.; Schedin, F.; Ponomarenko, L. A.; Morozov, S. V; Gleeson, H. F.; Hill, E. W.; Geim, A. K.; Novoselov, K. S. Graphene-Based Liquid Crystal Device. *Nano Lett.* **2008**, *8*, 1704–1708.

(8) Xu, Y.; Bai, H.; Lu, G.; Li, C.; Shi, G. Flexible Graphene Films via the Filtration of Water-Soluble Noncovalent Functionalized Graphene Sheets. *Journal of the American Chemical*

Society **2008**, *130*, 5856–5857.

(9) El-Kady, M. F.; Veronica Strong; Dubin, S.; Kaner, R. B. Laser Scribing of High-Performance and Flexible Graphene-Based Electrochemical Capacitors. *Science* **2012**, *335*, 1326–1330.

(10) Fowler, J. D.; Allen, M. J.; Tung, V. C.; Yang, Y.; Kaner, R. B.; Weiller, B. H. Practical Chemical Sensors from Chemically Derived Graphene. *ACS Nano.* **2009**, *3*, 301–306.

(11) Schedin, F.; Geim, A. K.; Morozov, S. V.; Hill, E. W.; Blake, P.; Katsnelson, M. I.; Novoselov, K. S. Detection of Individual Gas Molecules Adsorbed on Graphene. *Nat. Mater.* **2007**, *6*, 652–655.

(12) Bae, S. H.; Lee, Y.; Sharma, B. K.; Lee, H. J.; Kim, J. H.; Ahn, J. H. Graphene-Based Transparent Strain Sensor. *Carbon.* **2013**, *51*, 236–242.

(13) Sakhaee-Pour, A.; Ahmadian, M. T.; Vafai, A. Potential Application of Single-Layered Graphene Sheet as Strain Sensor. *Solid State Commun.* **2008**, *147*, 336–340.

(14) Schwierz, F. Graphene Transistors. *Nat. Nanotechnol.* **2010**, *5*, 487–496.

(15) Castro Neto, A. H.; Guinea, F.; Peres, N. M. R.; Novoselov, K. S.; Geim, A. K. The Electronic Properties of Graphene. *Rev. Mod. Phys.* **2009**, *81*, 109–162.

(16) Zhang, Y.; Tang, T.-T.; Girit, C.; Hao, Z.; Martin, M. C.; Zettl, A.; Crommie, M. F.; Shen, Y. R.; Wang, F. Direct Observation of a Widely Tunable Bandgap in Bilayer Graphene. *Nature* **2009**, *459*, 820–823.

(17) Han, M. Y.; Ozyilmaz, B.; Zhang, Y.; Kim, P. Energy Band-Gap Engineering of Graphene Nanoribbons. *Phys. Rev. Lett.* **2007**, *98*, 1–4.

(18) Zhou, S. Y.; Gweon, G.-H.; Fedorov, A. V.; First, P. N.; Heer, W. A. de; Lee, D.-H.; Guinea, F.; Neto, A. H. C.; Lanzara, A. Substrate-Induced Band Gap Opening in Epitaxial Graphene. *Nat. Mater.* **2007**, *6*, 770–775.

(19) Lopez-Sanchez, O.; Lembke, D.; Kayci, M.; Radenovic, A.; Kis, A. Ultrasensitive Photodetectors Based on Monolayer MoS_2. *Nat. Nanotechnol.* **2013**, *8*, 497–501.

(20) Kufer, D.; Konstantatos, G. Highly Sensitive, Encapsulated MoS_2 Photodetector with Gate Controllable Gain and Speed. *Nano Lett.* **2015**, 15, 7307-7313.

(21) Sliney, H. E. Solid Lubricant Materials for High Temperatures-a Review. *Tribol. Int.* **1982**, *15*, 303–315.

(22) Wang, Y.; Cong, C.; Yang, W.; Shang, J.; Peimyoo, N.; Chen, Y.; Kang, J.; Wang, J.; Huang, W.; Yu, T. Strain-Induced Direct-Indirect Bandgap Transition and Phonon Modulation in Monolayer WS_2. *Nano Res.* **2015**, *8*, 2562–2572.

(23) Elías, A. L.; Perea-López, N.; Castro-Beltrán, A.; Berkdemir, A.; Lv, R.; Feng, S.; Long, A. D.; Hayashi, T.; Kim, Y. A.; Endo, M.; Gutiérrez, H.; Pradhan, N. R.; Balicas, L.; Mallouk, T. E.; López-Urías, F.; Terrones, H.; Terrones, M. Controlled Synthesis and Transfer of Large-Area WS_2 Sheets: From Single Layer to Few Layers. *ACS Nano.* **2013**, *7*, 5235–5242.

(24) Tan, H.; Fan, Y.; Zhou, Y.; Chen, Q.; Xu, W.; Warner, J. H. Ultrathin 2D Photodetectors Utilizing Chemical Vapor Deposition Grown WS_2 with Graphene Electrodes. *ACS Nano.* **2016**, *10*, 7866–7873.

(25) Lee, C.-H.; Lee, G.; van der Zande, A. M.; Chen, W.; Li, Y.; Han, M.; Cui, X.; Arefe, G.; Nuckolls, C.; Heinz, T. F.; Guo, J.; Hone, J.; Kim, P. Atomically Thin p-n Junctions with van Der Waals Heterointerfaces. *Nat. Nanotechnol.* **2014**, *9*, 676–681.

(26) Zhang, C.; Xie, Y.; Deng, H.; Tumlin, T.; Zhang, C.; Su, J.-W.; Yu, P.; Lin, J. Monolithic and Flexible ZnS/SnO_2 Ultraviolet Photodetectors with Lateral Graphene Electrodes. *Small* **2017**, 13, *1604197*.

(27) Roy, T.; Tosun, M.; Kang, J. S.; Sachid, A. B.; Desai, S. B.; Hettick, M.; Hu, C. C.; Javey, A. Field-Effect Transistors Built from All Two-Dimensional Material Components. *ACS Nano.* **2014**, *8*, 6259–6264.

(28) Britnell, L.; Ribeiro, R. M.; Eckmann, A.; Jalil, R.; Belle, B. D.; Mishchenko, A.; Kim, Y.; Gorbachev, R. V; Georgiou, T.; Morozov, S. V; Grigorenko, A. N.; Geim, A. K.; Casiraghi, C.; Neto, A. H. Castro.; Novoselov, K. S. Strong Light-Matter Interactions in Heterostructures of Atomically Thin Films. *Science* **2013**, *340*, 1331–1314.

(29) Yu, W. J.; Vu, Q. A.; Oh, H.; Nam, H. G.; Zhou, H.; Cha, S.; Kim, J.-Y.; Carvalho, A.; Jeong, M.; Choi, H.; Neto, A. H. Castro.; Lee, Y. H.; Duan, X. Unusually Efficient Photocurrent Extraction in Monolayer van Der Waals Heterostructure by Tunnelling through Discretized Barriers. *Nat. Commun.* **2016**, *7*, 13278.

(30) Yu, W. J.; Liu, Y.; Zhou, H.; Yin, A.; Li, Z.; Huang, Y.; Duan, X. Highly Efficient Gate-Tunable Photocurrent Generation in Vertical Heterostructures of Layered Materials. *Nat. Nanotechnol.* **2013**, *8*, 952–958.

(31) Wu, Y. A.; Fan, Y.; Speller, S.; Creeth, G. L.; Sadowski, J. T.; He, K.; Robertson, A. W.; Allen, C. S.; Warner, J. H. Large Single Crystals of Graphene on Melted Copper Using Chemical Vapor Deposition. *ACS Nano.* **2012**, *6*, 5010–5017.

(32) Zeng, H.; Liu, G.-B.; Dai, J.; Yan, Y.; Zhu, B.; He, R.; Xie, L.; Xu, S.; Chen, X.; Yao, W.; Cui, X. Optical Signature of Symmetry Variations and Spin-Valley Coupling in Atomically Thin Tungsten Dichalcogenides. *Sci. Rep.* **2013**, *3*, 1608.

(33) He, Z.; Xu, W.; Zhou, Y.; Wang, X.; Sheng, Y.; Rong, Y.; Guo, S.; Zhang, J.; Smith, J. M.; Warner, J. H. Biexciton Formation in Bilayer Tungsten Disulfide. *ACS Nano* **2016**, *10*, 2176–2183.

(34) Tan, H.; Fan, Y.; Rong, Y.; Porter, B.; Lau, C. S.; Zhou, Y.; He, Z.; Wang, S.; Bhaskaran, H.; Warner, J. H. Doping Graphene Transistors Using Vertical Stacked Monolayer WS_2 Heterostructures Grown by Chemical Vapor Deposition. *ACS Appl. Mater. Interfaces.* **2016**, *8*, 1644–1652.

(35) Huo, N.; Wei, Z.; Meng, X.; Kang, J.; Wu, F.; Li, S.-S.; Wei, S.-H.; Li, J. Interlayer Coupling and Optoelectronic Properties of Ultrathin Two-Dimensional Heterostructures Based on Graphene, MoS_2 and WS_2. *J. Mater. Chem. C* **2015**, *3*, 5467–5473.

(36) Beebe, J. M.; Kim, B.; Gadzuk, J. W.; Frisbie, C. D.; Kushmerick, J. G. Transition from

Direct Tunneling to Field Emission in Metal-Molecule-Metal Junctions. *Phys. Rev. Lett.* **2006**, *97*, 1–4.

(37) Zhang, W.; Chuu, C.-P.; Huang, J.-K.; Chen, C.-H.; Tsai, M.-L.; Chang, Y.-H.; Liang, C.-T.; Chen, Y.-Z.; Chueh, Y.-L.; He, J.-H.; Chou, M.-Y.; Li, L.-J.; Ultrahigh-Gain Photodetectors Based on Atomically Thin Graphene-MoS_2 Heterostructures. *Sci. Rep.* **2014**, *4*, 3826.

(38) Bernardi, M.; Palummo, M.; Grossman, J. C. Extraordinary Sunlight Absorption and One Nanometer Thick Photovoltaics Using Two-Dimensional Monolayer Materials. *Nano Lett.* **2013**, *13*, 3664–3670.

(39) Chu, T.; Ilatikhameneh, H.; Klimeck, G.; Rahman, R.; Chen, Z. Electrically Tunable Bandgaps in Bilayer MoS_2. *Nano Lett.* **2015**, *15*, 8000–8007.

(40) Steinleitner, P.; Merkl, P.; Nagler, P.; Mornhinweg, J.; Schüller, C.; Korn, T.; Chernikov, A.; Huber, R. Direct Observation of Ultrafast Exciton Formation in a Monolayer of WSe_2. *Nano Lett.* **2017**, *17*, 1455–1460.

(41) Ceballos, F.; Cui, Q.; Bellus, M. Z.; Zhao, H. Exciton Formation in Monolayer Transition Metal Dichalcogenides. *Nanoscale* **2016**, *8*, 11681–11688.

(42) Zhu, B.; Chen, X.; Cui, X. Exciton Binding Energy of Monolayer WS_2. *Sci Rep.* **2015**, *5*, 9218 .

(43) Ye, Z.; Cao, T.; O'Brien, K.; Zhu, H.; Yin, X.; Wang, Y.; Louie, S. G.; Zhang, X. Probing Excitonic Dark States in Single-Layer Tungsten Disulphide. *Nature*. **2014**, *513*, 214–218.

(44) Guo, Y.; Sun, D.; Ouyang, B.; Raja, A.; Song, J.; Heinz, T. F.; Brus, L. E. Probing the Dynamics of the Metallic-to-Semiconducting Structural Phase Transformation in MoS_2 Crystals. *Nano Lett.* **2015**, *15*, 5081-5088.

(45) Luong, D. H.; Lee, H. S.; Neupane, G. P.; Roy, S.; Ghimire, G.; Lee, J. H.; Vu, Q. A.; Lee, Y. H. Tunneling Photocurrent Assisted by Interlayer Excitons in Staggered van Der Waals Hetero-Bilayers. *Adv. Mater.* **2017**, *1701512*, 1–8.

(46) He, Z.; Sheng, Y.; Rong, Y., Lee, G. D.; Li, J.; Warner, J. H. Layer-dependent modulation of tungsten disulfide photoluminescence by lateral electric fields. *ACS nano* **2015**, *9(3)*, 2740–2748.

(47) Borzda, T.; Gadermaier, C.; Vujicic, N.; Topolovsek, P.; Borovsak, M.; Mertelj, T.; Antognazza, M. R. Charge Photogeneration in Few-Layer MoS_2. *Adv. Funct. Mater.* **2015**, *25(22)*, 3351–3358.

(48) Azhikodan, D.; Nautiyal, T.; Shallcross, S.; Sharma, S. An anomalous interlayer exciton in MoS_2. *Sci rep*, 2016, *6*.

(49) Rivera, P.; Schaibley, J. R.; Jones, A. M.; Ross, J. S.; Wu, S.; Aivazian, G.; Klement, P.; Ghimire, N. J.; Yan, J.; Mandrus, D. G. Observation of Long-Lived Interlayer Excitons in Monolayer $MoSe_2$-WSe_2 Heterostructures. *Nat. Commun*, **2015**, *6*, 6242.

(50) Gabor, N. M.; Song, J. C. W.; Ma, Q.; Nair, N. L.; Taychatanapat, T.; Watanabe, K.;

Taniguchi, Takashi.; Levitov, L. S.; Jarillo-Herrero, P. Hot carrier-assisted intrinsic photoresponse in graphene. *Science*, **2011**, *334(6056)*, 648–652.

(51) Xu, X.; Gabor, N. M.; Alden, J. S.; Van der Zande, A. M.; McEuen, P. L. Photo-thermoelectric effect at a graphene interface junction. *Nano Lett*. **2009**,*10(2)*, 562–566.

TOC graphic